

# Reconsidering the consistent use of precessing, higher order multipole models for gravitational wave analyses

C. Hoy<sup>1</sup>\*

<sup>1</sup>*Institute of Cosmology and Gravitation, University of Portsmouth, Portsmouth, PO1 3FX, UK*

Accepted XX. Received YY; in original form ZZ

## ABSTRACT

The growing number of gravitational-wave (GW) observations allows for constraints to be placed on the underlying population of black holes; current estimates show that black hole spins are small, with binaries more likely to have comparable component masses. Since general relativistic effects, such as spin-induced orbital precession and higher order multipole moments, are more likely to be observed for asymmetric binary systems, a direct measurement remains unlikely. Nevertheless, we continue to consistently probe these effects by performing Bayesian inference with our most accurate and computationally expensive models. As the number of GW detections increases, it may soon become infeasible to consistently use these models for analyses. In this paper, we provide a selection criterion that determines when less accurate and computationally cheaper models can be used without giving biased estimates for the population properties of black holes in the Universe. We show that when using our selection criterion, comparable estimates can be obtained for the underlying mass and spin distribution of black holes for a simulated “worst-case” scenario population, while reducing the overall cost of performing Bayesian inference on our population by  $\sim 20\%$ . We anticipate a reduction of up to 78% in the overall cost for an astrophysically motivated population, since there are fewer events with observable spin-precession and higher order multipole power.

**Key words:** gravitational waves – methods: data analysis – stars: black holes – black hole mergers

## 1 INTRODUCTION

The Advanced LIGO (Aasi et al. 2015), Virgo (Acernese et al. 2015) and KAGRA (Akutsu et al. 2021) gravitational-wave (GW) detectors have observed more than 200 signals from compact binary coalescences (Abac et al. 2025a). Through a combination of Bayesian methods and highly accurate GW models (see e.g. Abac et al. 2025b), estimates for the individual source properties can be obtained, and combined to understand the underlying population properties of black holes in the Universe (Abac et al. 2025c).

By combining the information from 158 GW signals, Abac et al. (2025c) demonstrated that black holes have non-extremal spins ( $\chi \sim 0.2$ ) that are preferentially aligned with the binaries orbit. They further highlighted that binary black holes are more likely to have equal component masses. Combined, this means that general relativistic effects – such as spin-induced orbital precession and higher order multipoles – are unlikely to be observed in GW signals. Spin-

induced orbital precession occurs when the binary’s spin is misaligned with the orbital angular momentum (Apostolatos et al. 1994), leaving characteristic amplitude and phase modulations in the emitted GW signal. Spin-precession is more likely to be observed in binaries with asymmetric component masses and large spin magnitudes (Fairhurst et al. 2020a,b). Higher order multipole moments (Goldberg et al. 1967; Thorne 1980) describe the amount of GW radiation emitted in a particular direction. The majority of power is emitted in the  $(\ell, m) = (2, 2)$  quadrupole, but for asymmetric component masses higher order terms become observable in the GW signal (Mills & Fairhurst 2021). Hoy et al. (2025b) demonstrated that up to the third GW observing run, only one event showed substantial evidence for precession: GW200129\_065458 (Abbott et al. 2023b; Hannam et al. 2022), and two events show substantial evidence for higher order multipoles: GW190412 (Abbott et al. 2020a) and GW190814 (Abbott et al. 2020b). Since then, other events may have shown signs of precession and higher order multipoles (Abac et al. 2025a).

Although there is a low probability of observing gen-

\* charlie.hoy@port.ac.uk

eral relativistic effects in a given signal (1 in 50 for spin-precession and 1 in 70 for higher order multipoles, see Hoy et al. 2025b), the majority of GW observations to date<sup>1</sup> are consistently analysed with models that incorporate spin-precession and higher order multipole moments (Nitz et al. 2023; Abbott et al. 2024, 2023b; Olsen et al. 2022; Mehta et al. 2025; Abac et al. 2025a). This is natural since they more accurately describe numerical solutions to general relativity (see e.g. Mac Uilliam et al. 2024; Varma et al. 2019a; Estellés et al. 2025; Hamilton et al. 2025) and, as a result, they are less likely to produce biased source estimates (see e.g. Calderón Bustillo et al. 2016; Ramos-Buades et al. 2023; Thompson et al. 2024; Yelikar et al. 2024; Mac Uilliam et al. 2024; Dhani et al. 2025; Akçay et al. 2025). However, when there is no measurable spin-precession and higher order multipole power in the observed signal, comparable estimates for the individual and collective properties of black holes are generally expected regardless of the physics included in the model. Indeed, Hoy & Leyde (2025) demonstrated that the inferred expansion rate of the universe remains agnostic to the physics included in the waveform model, and Singh et al. (2024) demonstrated that neglecting higher order multipoles does not bias population inference. Given that simpler and less accurate models can reduce the computational cost of Bayesian analyses by six times (on average, Hoy & Leyde 2025), a trivial method to reduce the growing computational cost of GW data analyses is to strategically use computationally cheaper models where possible.

In this work, we demonstrate that precessing, higher order multipole models do not need to be consistently used when analysing GW signals; rather, a combination of models can be used and comparable estimates for the underlying mass and spin distribution of black holes can be obtained. We propose a simple selection criterion that only uses computationally expensive and highly accurate models when known general relativistic effects are measurable in the observed signal; otherwise, computationally cheaper models that exclude spin-precession and/or higher order multipoles can be employed. We verify our selection criterion for a population of rapidly spinning black holes with a preference for asymmetric component masses; this non-astrophysically motivated population acts as a worse-case scenario where spin-precession and higher order multipole power is likely to be observed in a given GW signal. Based on our population, we estimate that our selection criterion reduces the overall cost of performing GW data analysis by at least  $\sim 20\%$  without employing likelihood accelerated techniques (Cornish 2010; Canizares et al. 2013, 2015; Smith et al. 2016; Vinciguerra et al. 2017; Zackay et al. 2018; Qi & Raymond 2021; Cornish 2021; Morisaki 2021; Morisaki et al. 2023; Krishna et al. 2023). Given that  $> 90\%$  of observed binary black holes have lower spin magnitudes and more symmetric component masses, an astrophysically motivated population

<sup>1</sup> For GW candidates that likely originate from binary black hole mergers, it is standard to use models that incorporate spin-precession and higher order multipole moments. For neutron star black hole or binary neutron star mergers, models that incorporate tidal effects are used. Often these do not include spin-precession or higher order multipoles contributions (see e.g. Dietrich et al. 2019; Thompson et al. 2020; Matas et al. 2020).

will obtain larger efficiencies, and can likely use a stricter selection criterion without incurring biases.

This paper is structured as follows: in Sec. 2 we provide an overview of spin-induced orbital precession and higher order multipoles, and discuss the impact of neglecting these phenomena in models and parameter estimation. In Sec. 3 we describe our selection criterion and verify it in Sec. 4. We finally conclude in Sec. 5.

## 2 OBSERVABLE GENERAL RELATIVISTIC EFFECTS

### 2.1 Spin-induced orbital precession

In general relativity, a compact binary coalescence on a quasi-circular orbit is described by fifteen parameters: eight describing the intrinsic properties of the source – the compact masses,  $m_1$  and  $m_2$ , the spin vectors of each object,  $\mathbf{S}_1$  and  $\mathbf{S}_2$  – and seven describing the extrinsic properties – the luminosity distance, inclination angle, sky location, polarization, phase and coalescence time. The total angular momentum of the binary  $\mathbf{J}$  is defined as the sum of the orbital angular momentum  $\mathbf{L}$  and the total spin of binary  $\mathbf{S} = \mathbf{S}_1 + \mathbf{S}_2$ .

When  $\mathbf{S}$  is misaligned with  $\mathbf{L}$ , the binary undergoes the general relativistic phenomenon of spin-induced orbital precession. In most cases,  $\mathbf{L}$  precesses around the approximately constant  $\mathbf{J}$  with an opening angle  $\beta$ . The strength of precession is described by the magnitude of the opening angle, with more prominent effects occurring for larger angles (Apostolatos et al. 1994).  $\beta$  is primarily determined by the total spin perpendicular to  $\mathbf{L}$ . For this reason, it is often convenient to define the effective perpendicular spin as,

$$\chi_p = \frac{1}{A_1} \max(A_1 \chi_1 \sin \theta_1, A_2 \chi_2 \sin \theta_2), \quad (1)$$

where  $A_1 = 2 + 3m_2/(2m_1)$ ,  $A_2 = 2 + 3m_1/2m_2$ ,  $\chi_i = m_i^2 |\mathbf{S}_i|$ , and  $\cos(\theta_i) = \mathbf{S}_i \cdot \mathbf{L}$  (Schmidt et al. 2015).  $\chi_p$  is defined between 0 and 1, where 0 indicates a binary without spin-precession and 1 indicates maximal spin-precession. Other effective perpendicular spins have also been proposed in the past (Thomas et al. 2021; Gerosa et al. 2021; Hoy et al. 2025a). It is also useful to define the effective parallel spin as (Racine 2008; Ajith et al. 2011),

$$\chi_{\text{eff}} = \frac{m_1 \chi_1 \cos \theta_1 + m_2 \chi_2 \cos \theta_2}{m_1 + m_2}. \quad (2)$$

While  $\beta$  and  $\chi_p$  describe the intrinsic strength of precession, they are not sufficient to indicate whether it is observable given our GW detectors. This is because the characteristic amplitude and phase modulations associated with spin-induced orbital precession depend on the extrinsic properties of the source. The observability of spin-precession is described by the precession signal-to-noise ratio (SNR),  $\rho_p$  (Fairhurst et al. 2020a,b). In the absence of precession,  $\rho_p$  is expected to follow a  $\chi$  distribution with two degrees of freedom from Gaussian noise alone. As such, in 90% of GW signals with no observable precession,  $\rho_p < 2.1$ . This null distribution is conservative and, in some cases, may prefer lower SNRs (if informative priors are used, see Hoy et al. 2022, 2025b).

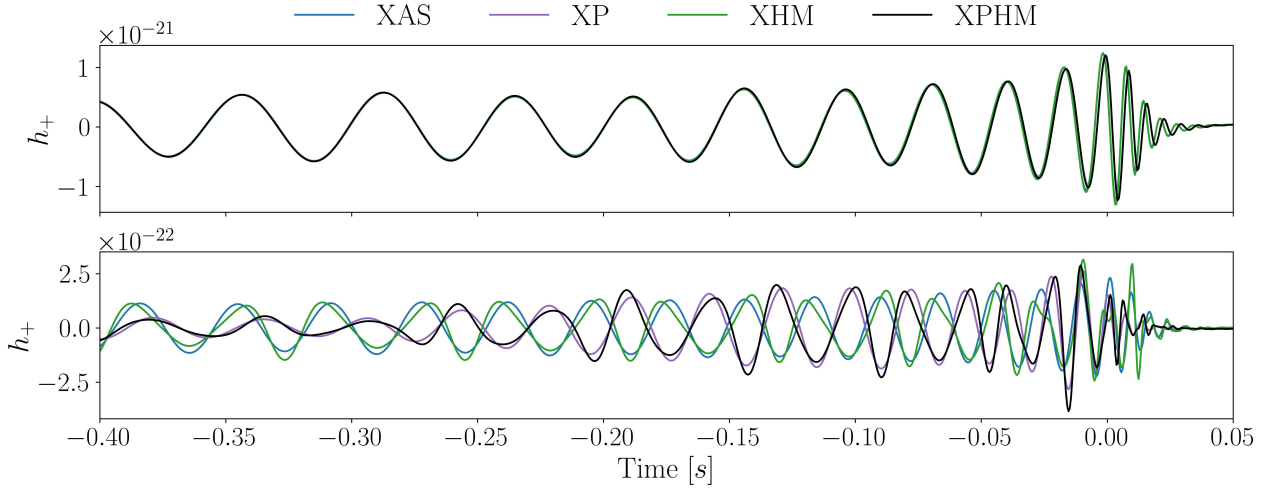


**Figure 1.** Plot showing the amplitude of the plus polarization,  $h_+$ , for two GW signals when assuming different physics; XAS assumes no spin-precession and higher order multipoles, XP assumes no higher order multipoles, XHM assumes no spin-precession, and XPHM includes both spin-precession and higher order multipoles. The *Top* panel compares the GW signals for an equal mass ratio binary with small spin magnitudes,  $\chi_1 = \chi_2 = 0.2$ , observed at an inclination angle of  $\pi/6$  rad. This represents a binary that is consistent with the observed population, and therefore likely to be detected by the LVK (Abac et al. 2025c). The *Bottom* panel compares the GW signals for a mass ratio  $q = 0.1$  binary with large spin magnitudes,  $\chi_1 = \chi_2 = 0.8$ , observed at an inclination angle of  $\pi/2$  rad.

## 2.2 Higher order multipole moments

The observed GW signal  $h = h_+ + ih_\times$  can be decomposed into an infinite sum of multipoles using  $-2$  spin-weighted spherical harmonics,  ${}^{-2}Y_{\ell,m}$  (Goldberg et al. 1967; Thorne 1980). Although the amplitude of each multipole varies across the parameter space, the  $(\ell, m) = (2, 2)$  quadrupole typically dominates the total power of the signal (Mills & Fairhurst 2021), albeit not always (Fairhurst et al. 2024; Ursell et al. 2025). The amplitude of each multipole depends on the total mass and mass ratio  $q = m_2/m_1$  of the binary, with the amplitude typically increasing for more asymmetric ( $q < 1$ ), higher total mass binaries (Mishra et al. 2016). For most cases, the  $(3, 3)$  multipole is the most significant higher order contribution after the quadrupole. Similar to spin-precession, the observability of each multipole can be described by an SNR,  $\rho_{\ell m}$  (Mills & Fairhurst 2021). We define  $\rho_{\text{PHM}}$  as the largest multipole SNR beyond the quadrupole.  $\rho_{\text{PHM}}$  is expected to follow the same null distribution as  $\rho_p$ .

## 2.3 Impact on models and parameter estimation

GW models are typically constructed from a combination of analytic and semi-analytic approximations, as well as fits to numerical relativity calculations (see e.g. Abac et al. 2025b). Since model development is a labour intensive process, models that neglect spin-precession and multipoles beyond the dominant quadrupole are often developed first. In subsequent years, additional physics is added to more reliably describe numerical solutions to general relativity at the expense of computational efficiency. Numerous model families are available, with the LIGO–Virgo–KAGRA collaboration (LVK) typically using the **Phenom** (Husa et al. 2016; Khan et al. 2016; London et al. 2018; Hannam et al. 2014; Khan et al. 2019, 2020; Pratten et al. 2020b; García-Quirós et al. 2020; Pratten et al. 2021; Estellés et al.

2021, 2022a,b; Hamilton et al. 2021; Thompson et al. 2024; Colleoni et al. 2025; Hamilton et al. 2025), **SEOBNR** (Bohé et al. 2017; Cotesta et al. 2018, 2020; Ossokine et al. 2020; Babak et al. 2017; Pan et al. 2014; Pompili et al. 2023; Ramos-Buades et al. 2023; Gamboa et al. 2025) and **NRSurrogate** (Varma et al. 2019b,a) families. Focusing on the “X” generation of **Phenom** waveforms, a GW signal from a quasi-circular binary black hole can be described by (i) **PhenomXAS** (XAS) when neglecting spin precession and higher order multipoles (Pratten et al. 2020b), (ii) **PhenomXP** (XP) when neglecting higher order multipoles (Pratten et al. 2021), (iii) **PhenomXHM** (XHM) when neglecting spin-precession (García-Quirós et al. 2020) and, (iv) **PhenomXPHM** (XPHM) otherwise (Pratten et al. 2021). On average<sup>2</sup> XPHM is  $1.2 \times$  slower than XAS,  $1.1 \times$  slower than XP, and  $1.2 \times$  slower than XHM for a single waveform evaluation.

Since both the intrinsic and extrinsic properties of the source affect the observability of spin-precession and higher order multipoles in the detected signal, the intrinsic  $\rho_p$  and  $\rho_{\text{PHM}}$  can be approximately zero for certain configurations. For these cases, a GW signal produced with XPHM is indistinguishable from XAS (see e.g. Thompson et al. 2025, for details on indistinguishability in the GW context, and its dependence on the SNR of the signal); in other words, there is little advantage in using more computationally expensive models to describe the observed GW signal. This is shown in the top panel of Fig. 1. We see that for a binary typically observed by the LVK (Abac et al. 2025c)

<sup>2</sup> We averaged over 5000 waveform evaluations with chirp masses in the range  $2 < \mathcal{M} < 200$  and mass ratios in the range  $0.05 < q < 1$ . We chose the duration of each waveform evaluation based on the component masses and spins. We consistently used a maximum frequency of 1024 Hz and a sampling frequency of 2048 Hz.

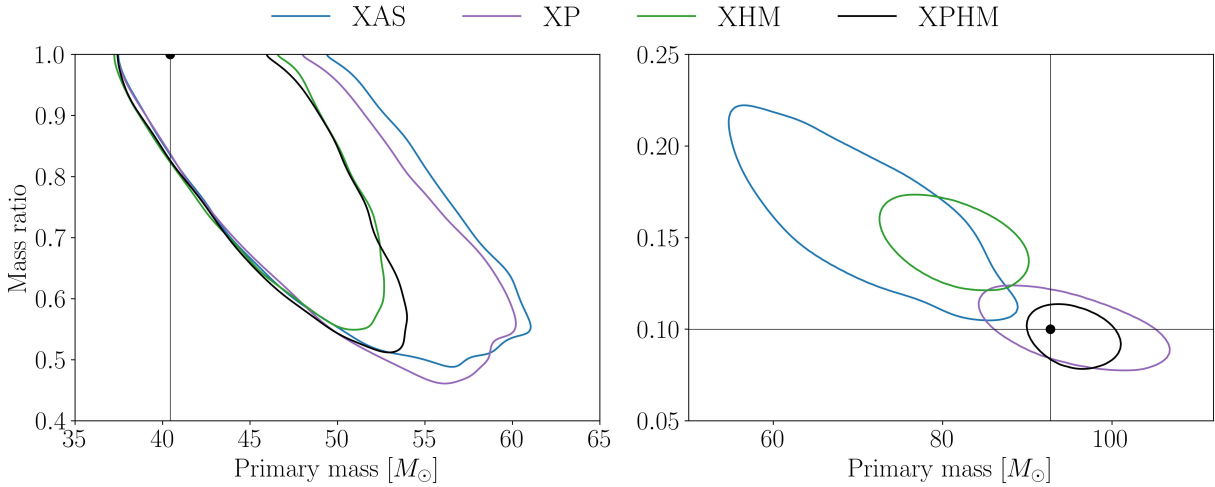


**Figure 2.** Plot showing the inferred primary mass and mass ratio when performing Bayesian inference on the GW signals shown in Fig. 1. We inject each GW signal into LIGO-Hanford and LIGO-Livingston, operating at their design sensitivities (Aasi et al. 2015). The *Left* panel corresponds to a GW signal with no observable precession and higher order multipoles, the *Top* panel in Fig. 1. The *Right* panel corresponds to a GW signal with observable precession and higher order multipoles, the *Bottom* panel in Fig. 1. In both cases we inject a simulated GW signal produced with XPHM into idealised Gaussian noise, and perform inference with XAS, XP, XHM and XPHM. The black cross hairs show the true values. The contours show the inferred 90% credible interval.

– an equal mass ratio binary with small spin magnitudes ( $\chi_1 = \chi_2 = 0.2$ ),  $\rho_p = 0.5$ ,  $\rho_{\text{HM}} = 0.5$ , and observed at a total network SNR of 20 – the predicted GW signals from different models are indistinguishable, despite missing key physical effects in most cases. Although demonstrated with the `Phenom` family, the same result would be obtained with `SEOBNR` and `NRSurrogate`. Of course, this is not always the case. For a binary with significant evidence for spin-precession and higher order multipoles,  $\rho_p, \rho_{\text{HM}} > 2.1$ , we see significant differences in the GW signals, as shown in the bottom panel of Fig. 1. To observe this level of disagreement requires extreme binary configurations that are unlikely to be observed given current expectations for the mass and spin distribution of black holes in the Universe (Abac et al. 2025c) – here we show a mass ratio  $q = 0.1$  binary with large spin magnitudes ( $\chi_1 = \chi_2 = 0.8$ ),  $\rho_p = 7.9$ ,  $\rho_{\text{HM}} = 7.8$ , and observed at a total network SNR of 20.

As our ability to infer the *true* source properties from an observed GW signal depends on the chosen model (see Abac et al. 2025b, and App. A1 for details), we expect to obtain comparable source estimates when analysing a GW signal with no evidence for spin-precession and higher order multipole moments regardless of the model used. We note that for some cases, the lack of evidence for precession and higher order multipoles can help further constrain the parameters. GW190814 (Abbott et al. 2020b) clearly demonstrates this: the lack of evidence for precession reduces the uncertainty in the inferred mass of the secondary object from  $2.4 - 2.8 M_\odot$  to  $2.5 - 2.7 M_\odot$  (at the 90% credible interval), see Fig. 4 in Abbott et al. (2020b). Although the uncertainties can shrink, the median is often comparable. This becomes more relevant for signals with large total power.

To demonstrate that we obtain comparable source estimates when there is no evidence for precession and higher order multipoles in the signal, we inject the XPHM signal shown in the top panel of Fig. 1 into idealised Gaus-

sian noise for a network of 2 advanced LIGO (Aasi et al. 2015) detectors. We then perform Bayesian inference with the `dynesty` (Speagle 2020) nested sampler via `bilby` (Ashdown et al. 2019; Romero-Shaw et al. 2020) with XAS, XP, XHM and XPHM. In all cases, we ensure wide and agnostic priors for all parameters and 2000 live points to ensure robust results; further details can be found in App. A1. In the left panel of Fig. 2 we show the two-dimensional marginalized posterior distribution for  $m_1$  and  $q$ . We see that we obtain comparable estimates for source properties regardless of the model used, as expected. This is despite XAS, XP and XHM using  $5\times$ ,  $2\times$  and  $4\times$  less computational resources than XPHM respectively<sup>3</sup>. When performing model selection, see App. A1 for details, we see that the  $\log_{10}$  Bayes factor's between the different models are less than 1, highlighting no model preference. Hoy & Leyde (2025) demonstrated that across a population of simulated signals, XAS uses on average  $6\times$  less computational resources than XPHM. The exact computational cost varies for each signal as it depends on priors, data durations, frequencies considered etc.

For cases where we observe large differences between predicted signals produced with different models, *i.e.* for binaries with significant evidence for spin-precession and higher order multipoles, we expect to observe biases in the source properties when employing models that neglect physics. This is shown in the right hand panel of Fig. 2. We see that when injecting the XPHM signal shown in the bottom panel of Fig. 1 into idealised Gaussian noise

<sup>3</sup> Although a single waveform evaluation for *e.g.* XAS is only  $1.2\times$  faster than XPHM,  $\mathcal{O}(10^7)$  waveform evaluations are performed in a typical Bayesian analysis, hence the significant reduction in computational resources. XAS also explores a reduced parameter space, due to neglecting in-plane spin components. This also contributes to the reduction in computational cost.

and recovering with XAS, XHM, XP and XPHM, XAS and XHM recover a biased primary mass and mass ratio. XP and XPHM recover the true values within the inferred 90% credible interval, implying that neglecting higher order contributions to the total signal power is key to biasing our inference. This is well known and has been previously demonstrated (see e.g. Chatzioannou et al. 2015; Pürer et al. 2016; Calderón Bustillo et al. 2016; London et al. 2018; Cotesta et al. 2018; Kalaghatgi et al. 2020; Pratten et al. 2020a; García-Quirós et al. 2020; Krishnendu & Ohme 2022). This is supported by  $\log_{10}$  Bayes factor's between the different models; XPHM is preferred over XAS with a  $\log_{10} \mathcal{B} = 40$ .

### 3 DETERMINING THE SELECTION FUNCTION

Based on the results in Sec. 2, a trivial method for reducing the computational cost of performing Bayesian inference for a population of GW signals (without employing any new techniques) is to design a selection function that strategically uses XAS when there is no evidence for precession and higher order multipoles in the detected signal, and XP (XHM) when there is significant evidence for precession (higher order multipoles). This means that we only use the most computationally expensive model, XPHM, for the few signals where necessary. By using only models that contain sufficient physics to describe the observed signal, biases can be controlled, and computational cost reduced. Based on Figs. 1 and 2, a natural strategy is to set an SNR threshold based on  $\rho_p$  and  $\rho_{HM}$ ; if  $\rho_p$  and  $\rho_{HM}$  are small, XAS is sufficient to describe the signal, while if  $\rho_p$  and  $\rho_{HM}$  are large, XPHM is essential. Of course, this requires an estimate for  $\rho_p$  and  $\rho_{HM}$  *a priori*.

Fairhurst et al. (2023) demonstrated that `simple-pe` can directly extract  $\rho_p$  and  $\rho_{HM}$  from the GW strain data through matched filtering (Brown 2004), within seconds on a single CPU. The process is as follows: first, the best fitting dominant quadrupole-only waveform that maximises the matched filter SNR of the observed signal is identified through an optimisation step. A similar strategy has also been employed in low-latency searches (Nitz et al. 2018). This *template* is split into a series orthogonal components, with each describing the isolated contribution from precession (Fairhurst et al. 2020a) and higher order multipoles Mills & Fairhurst (2021); Fairhurst et al. (2023). Each component is then matched filtered against the data to obtain an SNR. A similar procedure has been implemented in PyCBC (Usman et al. 2016) to search for precessing binaries (McIsaac et al. 2023; Harry & Hoy 2025).

It is important to choose a selection function that *e.g.* ensures XAS is only used for analyses when there is no evidence for precession and higher order multipoles in the signal. Otherwise, biases are expected, see Fig. 2. Therefore, we first compare the matched filtered  $\rho_p$  and  $\rho_{HM}$  against the true SNRs to identify whether they can reliably be used to define a threshold. We are only interested in false negatives: cases where we identify the signal with no evidence for precession and/or higher order multipoles despite the true signal showing strong observable features. False negatives imply that we may select a model that is insufficient

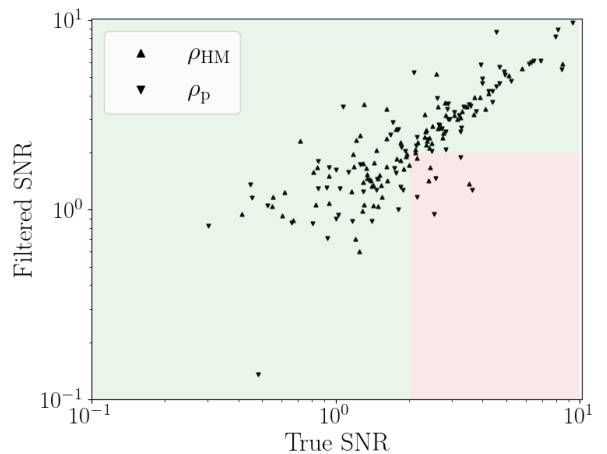


**Figure 3.** Plot comparing the matched filtered SNR in precession  $\rho_p$  and higher order multipoles  $\rho_{HM}$  to the true SNR for our worst-case scenario population. The shaded red region shows false negatives: a region where we identify the binary as having no evidence for precession and/or higher order multipoles from the filtered SNR despite there being observable features in the signal. The green region shows false positives, true positives and true negatives. We define  $\rho_p = \rho_{HM} = 2.0$  for a binary with significant evidence of precession and/or higher order multipoles.

to describe the signal. False positives are tolerable since this implies that a model with more physics than necessary will be used.

We simulate a *worst-case scenario* population of binary black holes: we consider a population of 90 binary black holes with large spin magnitudes and isotropic spin tilts – leading to significant evidence for precession – with a preference for asymmetric masses – leading to significant evidence for higher order multipoles. The LVK has started to see evidence that these binaries may exist in nature (Abac et al. 2025f). We only draw binaries with observable GW signals given current detector networks. Rather than injecting signals into real GW data and performing a search to identify which are detected (see e.g. Abac et al. 2025c, and App. A2 for details), we simplify the process by assuming signals with total signal power greater than 12 are observable (Essick 2023; Mould et al. 2024; Gerosa & Bellotti 2024; Agarwal et al. 2025; Hoy & Leyde 2025). We calculate that  $\sim 8\%$  of binaries drawn from the observed LVK population (Abac et al. 2025c) are included in our simulated population. We then generate GW signals for each binary merger with XPHM, and inject all into different realisations of idealised Gaussian noise for an Advanced LIGO and Advanced Virgo network operating at 75% duty cycle. We note that a population of 90 signals with total signal power greater than 12 remains more than all loud signals observed up to the first part of the fourth observing run (Abac et al. 2025a). We consider this worst-case scenario population since it increases the number of GW signals with observable  $\rho_p$  and  $\rho_{HM}$  compared to current population expectations.

We obtain our simulated population by assuming that the mass ratio follows a power law  $q^{\beta_q}$  with index  $\beta_q = -1.1$ , and spin magnitudes follow a truncated Gaussian distribution with mean  $a_i = 0.7$  and standard deviation  $\sigma = 0.2$ . We also assume that the primary mass follows a truncated

power law with index  $\alpha = -2.3$ , between a minimum,  $m_{\min} = 5 M_{\odot}$ , and maximum  $m_{\max} = 80 M_{\odot}$  mass. We assume that there is a Gaussian component in the mass distribution at  $m_1 = 34 M_{\odot}$ , with relative weight  $\lambda = 0.038$  and standard deviation  $\sigma_g = 5 M_{\odot}$ . This is the same simulated population used in [Hoy & Leyde \(2025\)](#) and inspired from previous LVK results ([Abbott et al. 2023a](#)).

As shown in Fig. 3, `simple-pe` approximately recovers the expected linear relationship between the true and matched filter SNRs, especially at large values ( $\text{SNR} \gtrsim 2$ ). This implies that we are unlikely to misidentify the signal when there is extreme evidence for spin-precession and higher order multipoles in the signal. At low SNRs, the linear relationship starts to break down, which is expected due to the presence of Gaussian noise. We see that if  $\rho_p = \rho_{\text{HM}} = 2.0$  corresponds to a binary with significant evidence of precession and/or higher order multipoles, only 6% of matched filter SNRs lead to false negatives, with most lying near the boundary. When repeating this analysis with the same simulations injected into *zero noise*<sup>4</sup>, we find that the number of false negatives decreases to 3%.

There are several false negatives where *e.g.* the true SNR is  $\sim 3.5$  while we obtain a matched filter SNR  $\sim 1.5$ . One of these has significant evidence spin-precession. Since we misidentify the significance of this signal, we specifically show the impact of the chosen model on the posterior for this event in App. C. We show that using a computationally cheaper model still recovers the true values within the 90% credible interval. This gives confidence that even if the signal is misidentified, we obtain reasonable parameter estimates.

Given that we consider a worst-case scenario population, we expect this to be an upper limit. Since the main driving force behind the false negatives seems to be a consequence of the specific Gaussian noise realisation chosen, we conclude that the matched filter  $\rho_p$  and  $\rho_{\text{HM}}$  are robust to define a SNR threshold.

#### 4 IDENTIFYING AN SNR THRESHOLD

Our aim is to define a selection function – and hence an SNR threshold for  $\rho_p$  and  $\rho_{\text{HM}}$  – such that when hierarchical Bayesian inference (see [Thrane & Talbot 2019](#), and App. A2 for details) is performed on a population of GW signals, the inferred mass and spin distribution of black holes remains unchanged. By doing so, this implies that our ability to extract key physics from our GW observations remains unaltered.

To identify a suitable threshold,  $\rho_{\text{thres}}$ , we analyse all 90 binary black holes in our simulated, worst-case scenario population described in Sec. 3 numerous times: first when consistently using XPHM for all single-event Bayesian analyses, and for the others: when using a model chosen from a threshold on the matched filtered  $\rho_p$  and  $\rho_{\text{HM}}$  from `simple-pe`. We chose 6 different thresholds,  $\rho_{\text{thres}} \in [0.5, 1.0, 1.5, 2.0, 2.5, 3.0]$ . We use,

- (i) XAS when  $\rho_p < \rho_{\text{thres}}$  and  $\rho_{\text{HM}} < \rho_{\text{thres}}$ ,
- (ii) XHM when  $\rho_p < \rho_{\text{thres}}$  and  $\rho_{\text{HM}} > \rho_{\text{thres}}$ ,

<sup>4</sup> The noise is set to its expectation value under infinite Gaussian noise realizations

- (iii) XP when  $\rho_p > \rho_{\text{thres}}$  and  $\rho_{\text{HM}} < \rho_{\text{thres}}$ ,
- (iv) XPHM when  $\rho_p > \rho_{\text{thres}}$  and  $\rho_{\text{HM}} > \rho_{\text{thres}}$ .

Using the posterior distributions obtained for each event, we perform hierarchical inference with the `dynesty` nested sampler via `gwpopulation` ([Talbot et al. 2019](#)), as is common ([Abac et al. 2025c](#)). We consistently assume a POWERLAW+PEAK model ([Abbott et al. 2021](#)) for the primary component mass, and a power law for the mass ratio distribution. We also assume that the component spin magnitudes are independently and identically drawn from a Beta distribution ([Wysocki et al. 2019](#)), and a mixture model comprising two components for the spin tilt is used: an isotropic component, and a second component in which the spins are preferentially aligned with **L** ([Talbot & Thrane 2018](#)). In all cases, we ensure wide and agnostic priors for all parameters and 1000 live points. More details are provided in App. A2.

An issue with combining single-event posterior distributions obtained with different models is that often alternative spin-priors are used; for models that neglect spin-precession (XAS and XHM) we typically use an aligned spin prior that is uniform in spin magnitude after marginalizing the in-plane spin contributions ([Lange et al. 2018](#)), while models that include spin-precession (XP and XPHM) typically use a uniform in spin magnitude prior. This results in XAS/XHM typically inferring lower spin magnitudes and exactly aligned (0) or anti-aligned ( $\pi$ ) spin-tilts, see Fig. 4. If naively combined with the posterior distributions obtained with XP and XPHM, biases are expected in the inferred spin-distribution of black holes. Similarly, we expect biases in the mass distribution due to the well known mass-spin degeneracy ([Baird et al. 2013](#)). To overcome this, we *predict* the in-plane spin distributions given the posteriors obtained with XAS and XHM.

In more detail, we re-weight the spin-magnitude distributions from the aligned-spin prior to a uniform in spin-magnitude prior. We then assume a uniform distribution for the spin-tilts (same as the one used for XP and XPHM) and condition them on the observed aligned-spin of the binary,  $\chi_{\text{eff}}$ . In Fig. 4, we show the result of this process. We see that after re-weighting and conditioning the XAS distributions, we obtain posteriors that are comparable to XPHM for signals with moderate observable precession and higher order multipoles. For this case,  $\rho_p = 2.0$  and  $\rho_{\text{HM}} = 0.6$ . However, this process breaks down when there is significant spin-precession in the GW signal. This is expected since our technique is essentially ignoring any measurable information from precession and, as a result, the inferred spin magnitudes are smaller and spin tilts more aligned. We note that this is not an issue in our analysis, as we propose only using XAS and XHM for signals without observable  $\rho_p$  and  $\rho_{\text{HM}}$ .

Our re-weighting and conditioning technique (applied to the XAS/XHM posteriors) is similar in principle to sampling over the priors used by XP and XPHM, and only considering the aligned-spin components during the inference. However, there will be small differences because our technique is sampling from a prior conditioned on the observed  $\chi_{\text{eff}}$ , rather than remaining agnostic. In our testing, our reweighting and conditioning algorithm obtained results that were more comparable to XPHM for the primary spin magnitude. An alternative, more robust, method could be to use Sequential Monte Carlo techniques ([Williams 2025](#)).

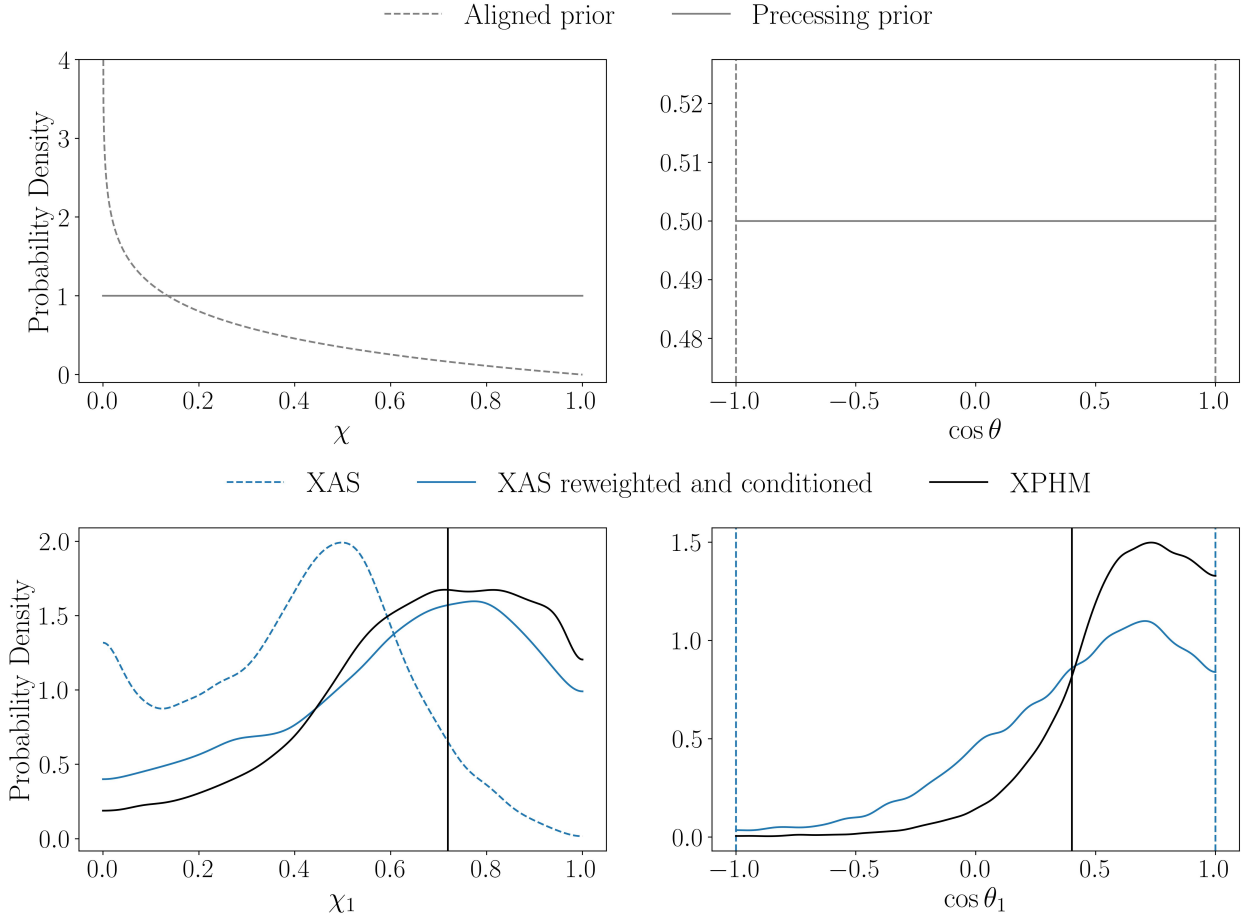


**Figure 4.** Plot showing the reweighting and conditioning procedure that is applied to the spin magnitude,  $\chi$ , and spin tilt,  $\cos \theta$ , posterior distributions obtained with XAS and XHM. The posterior distributions were obtained by analysing a simulated GW signal injected into idealised Gaussian noise. The binary had component masses  $m_1 = 34 M_\odot, m_2 = 34 M_\odot$ , spin magnitudes  $\chi_1 = 0.7, \chi_2 = 0.8$  and spin tilts  $\cos \theta_1 = 0.4, \cos \theta_2 = 0.3$ . The top row highlights the different spin-priors used for XAS/XHM (grey dash) and XPHM (grey solid). The bottom row compares the original XAS (blue dashed) and the XAS reweighted and conditioned posterior distribution (blue solid) with XPHM (black solid). In the bottom row, the black vertical line indicates with the true value.

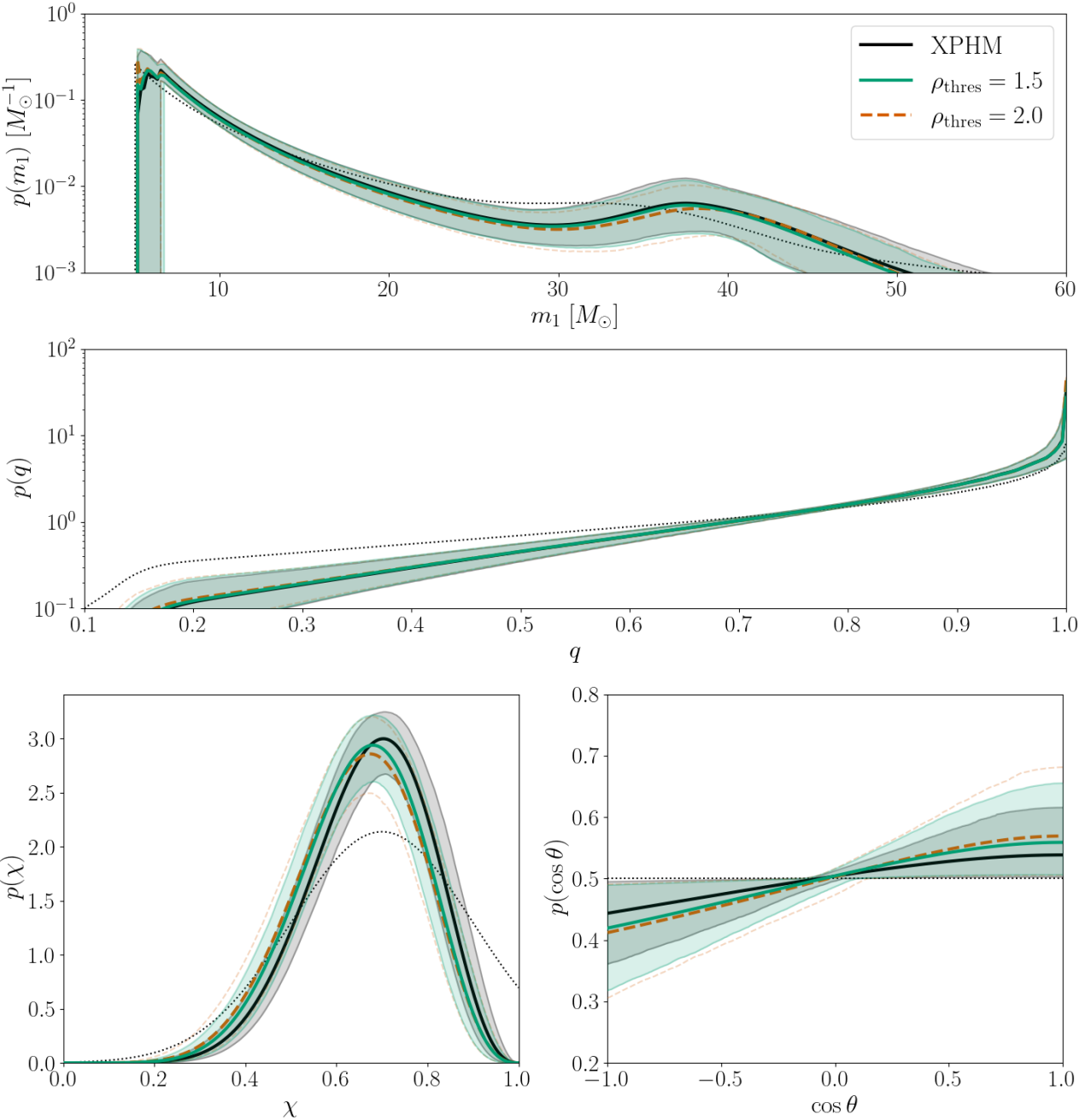
However, our re-weighting and conditioning algorithm uses significantly fewer computational resources and is sufficient for our need; our reweighting and conditioning technique takes  $\mathcal{O}(1)$  CPU minute to complete.

Fig. 5 shows our key result: when using a threshold of  $\rho_{\text{thres}} = 1.5$ , the inferred mass and spin distributions remain comparable to XPHM (within the 90% credible intervals), and the astrophysical understanding of black holes remains the same. We see that both distributions recover the properties of the injected population well, although there are some small discrepancies caused by the limited number of GW signals considered; we see that the inferred mass ratio distribution slightly underestimates the number of highly asymmetric component mass binaries ( $q \lesssim 0.15$ ), which is likely due to the random process of drawing 90 observable binary parameters from the simulated population. We also see that the spin peak is recovered well despite being modelled as a Beta distribution. However, it naturally goes to 0 at maximal spin, unlike the true truncated Gaussian. See App B.5.1 in Abac et al. (2025c) for a discussion of the limitations of the Beta distribution. A truncated Gaussian could have been used rather than a Beta distribution for inference

– to match the true simulated population – but we used a Beta distribution as it has been commonly used in the literature (see e.g. Abbott et al. 2021, 2023a). It is therefore expected that our inference did not recover the true spin distribution. We note that we obtain marginally more support for aligned spin binaries compared to XPHM.

The uncertainties on the inferred mass and spin distribution are expected to shrink if our simulated population contained  $\mathcal{O}(1000)$  binaries (Mould et al. 2025; Vitale & Mould 2025). However, we note that a population of this size may exhibit biases themselves owing to uncontrolled Monte-Carlo errors when evaluating the likelihood, see Es-sick & Farr (2022); Talbot & Golomb (2023); Heinzel & Vitale (2025) for details. As a result, even if a population of  $\mathcal{O}(1000)$  GW signals was observed, we may be forced to analyse a smaller number of higher SNR signals to control this growing error (Wolfe et al. 2025). Therefore, it is unlikely that the uncertainties will shrink enough to expose differences between XPHM and when imposing a selection threshold  $\rho_{\text{thres}} = 1.5$ . In the event that we suspect they will, a smaller threshold can be used.

From Fig. 6 we see that when using  $\rho_{\text{thres}} = 1.5$ , 4 events



**Figure 5.** Plot comparing the inferred mass and spin distribution for a simulated highly spinning population. The top and middle panels show the inferred distribution for the primary mass  $m_1$  and mass ratio  $q = m_2/m_1$  respectively. The bottom left and bottom right panels show the inferred spin magnitude,  $\chi$ , and spin orientation,  $\cos \theta$ , respectively. The black solid line shows the distribution inferred when solely using posterior samples obtained with XPHM. The green solid line shows the distribution inferred when using an SNR threshold of  $\rho_{\text{thres}} = 1.5$ , and the orange dashed line shows the distribution inferred when using a stricter SNR threshold of  $\rho_{\text{thres}} = 2.0$ . The dotted line shows the true distribution of the simulated population, and the bands show the inferred 90% credible intervals.

were analysed with XAS, 22 with XP, 24 with XHM and 38 with XPHM. We calculate that choosing the most sufficient and cheapest model to describe the observed signal reduces the overall cost of performing Bayesian inference on the population by  $\sim 20\%$ : a total of 40 CPU years compared to 50 CPU years when consistently using XPHM for all signals.

We see that when the SNR threshold is increased to  $\rho_{\text{thres}} = 2.0$ , noticeable differences are seen in the inferred

spin distribution, particularly in the 90% credible interval of the spin tilt with marginally more support for aligned spin binary's. This is despite the mass distribution remaining comparable to XPHM. Given that a greater number of GW signals will be analysed with XAS/XHM for a higher threshold, this is consistent with the re-weighing and conditioning process underestimating the true spin-magnitude and spin tilt distributions. This is more clearly seen in Fig. B1 in

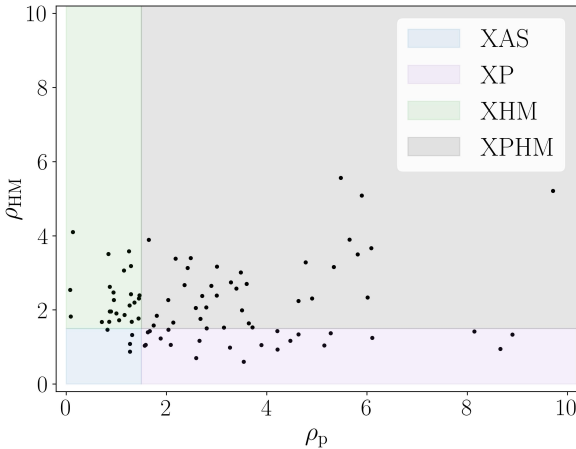


**Figure 6.** Plot showing the GW signals in our simulated, worst-case scenario population that were analysed by each model. We show this as a function of  $\rho_p$  and  $\rho_{\text{HM}}$ . We use the recommended SNR threshold of  $\rho_{\text{thres}} = 1.5$ .

App. B. As the threshold is further increased, more significant biases in the spin distribution is seen, with a preference for lower spin magnitudes and more aligned binaries. For this reason, although a threshold of  $\rho_{\text{thres}} = 2.0$  reduces the computational cost by  $\sim 25\%$ , we recommend using a maximum threshold of  $\rho_{\text{thres}} = 1.5$  to mitigate the risk of biased results.

## 5 DISCUSSION

In this work, we investigated a method for reducing the computational cost of performing Bayesian inference on a population of GW signals. Rather than consistently using highly accurate and computationally expensive models for GW analyses – as is the standard in the LVK and other work – we developed a selection function to determine when less accurate, and computationally cheaper models can be used without incurring biases in both single-event and hierarchical Bayesian analyses. We showed that by using an SNR threshold of  $\rho_{\text{thres}} = 1.5$  on the matched filtered  $\rho_p$  and  $\rho_{\text{HM}}$ , the inferred mass and spin distributions for a worse-case scenario population of binary black holes remain unchanged when compared to the consistent use of **PhenomXPHM**. For our population, we calculated that our selection function reduced the overall cost of performing Bayesian inference on the population by  $\sim 20\%$ . While we only investigated the impact on the inferred mass and spin distributions for black holes in the Universe, we expect our selection function to reduce the computational cost and obtain indistinguishable results when *e.g.* calculating the expansion rate of the Universe (Abac et al. 2025d) and identifying signatures of GW lensing (Abac et al. 2025e).

Although our current implementation involves obtaining the matched filter SNRs – and hence choosing the model – prior to sampling, it may be possible to include this calculation, and the selection function in the sampling itself, using the techniques developed in Hoy et al. (2025a). Similarly, although our SNR threshold determines when precession and higher order multipole power is not needed for inference, it

is possible that it could be extended to include eccentricity of the binaries orbit (Patterson et al. 2025; Singh et al. 2025).

Throughout this work, we assumed a worse-case scenario population. For an astrophysically motivated population (based on the GW observations from GWTC-4, Abac et al. 2025a), we expect to obtain larger efficiencies since  $> 90\%$  of observed binary black holes have lower spin magnitudes and more symmetric mass ratios where XAS is more likely to be selected. Even with the dominant usage of XAS, we expect to obtain consistent mass and spin distributions, see App. D for details. From Hoy et al. (2025b), 1 in 50 real GW signals show significant evidence for precession, and 1 in 70 events show significant evidence for higher order multipoles. As such, for a population of 500 real GW signals, we may expect to measure 10 events with significant evidence for precession and 8 with significant evidence for higher order multipoles. This implies that if our selection function was used, 482 events may be analysed with XAS without incurring any biases. This would reduce the overall cost of performing Bayesian inference on the population by up to 78% compared to consistently using XPHM. In the limit that we consistently use XAS compared to XPHM, we would expect a reduction in total cost of 83%.

GW models are constantly improving in their accuracy to numerical relativity simulations; **PhenomXPHM-SpinTaylor** (Colleoni et al. 2025), **PhenomX04a** (Thompson et al. 2024) and **PhenomXPNR** (Hamilton et al. 2025) all show improvements beyond **PhenomXPHM**. However, as shown in Fig. 14 of Hamilton et al. (2025), the waveform evaluation time typically increases with each successive improvement in the model. This means that by utilising our selection function, we expect the overall cost of performing Bayesian inference on the population to be reduced further with time.

Although the selection function described in this work is most suited for current and near-future detector networks (Iyer et al. 2011), it could be used alongside next generation detectors<sup>5</sup> (Punturo et al. 2010; Hild et al. 2011; Maggiore et al. 2020; Reitze et al. 2019; Babak et al. 2021; Colpi et al. 2024) – see Hoy et al. (2024) for a demonstration that a matched filtered  $\rho_{\text{HM}}$  can be extracted for signals observed with the Laser Interferometer Space Antenna (LISA, Colpi et al. 2024). However, it may not provide significant speed ups since GW signals observed in next generation detectors are expected to be detected at large SNRs. This implies that most observations will show significant  $\rho_p$  and  $\rho_{\text{HM}}$  (although the exact number depends on the unknown mass, spin and redshift distributions of the expected sources). As a result, in most cases, highly accurate models will be required to avoid biases.

## 6 ACKNOWLEDGMENTS

We are grateful to Mark Hannam for discussions and suggestions at the start of this project, Konstantin Leyde

<sup>5</sup> Unless novel methods are developed for performing Bayesian inference on GW data in  $\mathcal{O}(\text{sec})$ , such as machine learning algorithms (Green & Gair 2021; Green et al. 2020; Dax et al. 2021) or others (Fairhurst et al. 2023)

for conversations about hierarchical Bayesian inference and Matthew Mould for helpful comments during the LIGO-Virgo-KAGRA internal review. We thank Stephen Fairhurst, Ian Harry, Laura Nuttall and Mukesh Singh for valuable feedback on this manuscript. We additionally thank Stephen Fairhurst and Mukesh Singh for their continued development of `simple-pe` (alongside C.H.). We thank the University of Portsmouth for support through the Dennis Sciama Fellowship, and we are grateful for computational resources provided by the SCIMMA high performance computing cluster which is supported by the Institute of Cosmology and Gravitation (ICG) and the University of Portsmouth. For the purpose of open access, the author(s) has applied a Creative Commons Attribution (CC BY) licence to any Author Accepted Manuscript version arising.

Plots were prepared with Matplotlib (Hunter 2007), `pesummary` (Hoy & Raymond 2021) and `gwpopulation` (Talbot et al. 2019). Single-event parameter estimation was performed with `bilby` (Ashton et al. 2019; Romero-Shaw et al. 2020), and hierarchical parameter estimation was performed with `gwpopulation` (Talbot et al. 2019); both making use of the `dynesty` nesting sampling package (Speagle 2020). `simple-pe` (Fairhurst et al. 2023) and `pesummary` (Hoy & Raymond 2021) were used to extract the matched filter  $\rho_p$  and  $\rho_{\text{HM}}$  from the GW strain data. NumPy (Harris et al. 2020) and SciPy (Virtanen et al. 2020) were also used in our analyses.

## 7 DATA AVAILABILITY

Code to evaluate our selection function, as well as all posterior samples obtained in this work (both single-event and hierarchical analyses) are made publicly available on [GitHub](#).

## REFERENCES

Aasi J., et al., 2015, *Class. Quant. Grav.*, 32, 074001  
 Abac A. G., et al., 2025d, arXiv:2509.04348  
 Abac A. G., et al., 2025b, arXiv:2508.18081  
 Abac A. G., et al., 2025c, arXiv:2508.18083  
 Abac A. G., et al., 2025e, arXiv:2512.16347  
 Abac A. G., et al., 2025a, arXiv:2508.18082  
 Abac A. G., et al., 2025f, *Astrophys. J. Lett.*, 993, L21  
 Abbott R., et al., 2020a, *Phys. Rev. D*, 102, 043015  
 Abbott R., et al., 2020b, *Astrophys. J. Lett.*, 896, L44  
 Abbott R., et al., 2021, *Astrophys. J. Lett.*, 913, L7  
 Abbott R., et al., 2023a, *Phys. Rev. X*, 13, 011048  
 Abbott R., et al., 2023b, *Phys. Rev. X*, 13, 041039  
 Abbott R., et al., 2024, *Phys. Rev. D*, 109, 022001  
 Acernese F., et al., 2015, *Class. Quant. Grav.*, 32, 024001  
 Adams T., et al., 2016, *Class. Quant. Grav.*, 33, 175012  
 Agarwal A., et al., 2025, *Astrophys. J.*, 987, 47  
 Ajith P., et al., 2011, *Phys. Rev. Lett.*, 106, 241101  
 Akçay S., Hoy C., Mac William J., 2025, *Phys. Rev. D*, 112, 084032  
 Akutsu T., et al., 2021, *PTEP*, 2021, 05A101  
 Apostolatos T. A., Cutler C., Sussman G. J., Thorne K. S., 1994, *Phys. Rev. D*, 49, 6274  
 Ashton G., et al., 2019, *Astrophys. J. Suppl.*, 241, 27  
 Babak S., Taracchini A., Buonanno A., 2017, *Phys. Rev. D*, 95, 024010  
 Babak S., Petiteau A., Hewitson M., 2021, arXiv:2108.01167  
 Baird E., Fairhurst S., Hannam M., Murphy P., 2013, *Phys. Rev. D*, 87, 024035  
 Biwer C. M., Capano C. D., De S., Cabero M., Brown D. A., Nitz A. H., Raymond V., 2019, *Publ. Astron. Soc. Pac.*, 131, 024503  
 Bohé A., et al., 2017, *Phys. Rev. D*, 95, 044028  
 Brown D. A., 2004, Other thesis ([arXiv:0705.1514](#))  
 Calderón Bustillo J., Husa S., Sintes A. M., Pürrer M., 2016, *Phys. Rev. D*, 93, 084019  
 Canizares P., Field S. E., Gair J. R., Tiglio M., 2013, *Phys. Rev. D*, 87, 124005  
 Canizares P., Field S. E., Gair J., Raymond V., Smith R., Tiglio M., 2015, *Phys. Rev. Lett.*, 114, 071104  
 Cannon K., et al., 2012, *Astrophys. J.*, 748, 136  
 Chatzioannou K., Cornish N., Klein A., Yunes N., 2015, *Astrophys. J. Lett.*, 798, L17  
 Chu Q., et al., 2022, *Phys. Rev. D*, 105, 024023  
 Chua A. J. K., Vallisneri M., 2020, *Phys. Rev. Lett.*, 124, 041102  
 Colleoni M., Vidal F. A. R., García-Quirós C., Akçay S., Bera S., 2025, *Phys. Rev. D*, 111, 104019  
 Colpi M., et al., 2024, arXiv:2402.07571  
 Cornish N. J., 2010, arXiv:1007.4820  
 Cornish N. J., 2021, *Phys. Rev. D*, 104, 104054  
 Cotesta R., Buonanno A., Bohé A., Taracchini A., Hinder I., Ossokine S., 2018, *Phys. Rev. D*, 98, 084028  
 Cotesta R., Marsat S., Pürrer M., 2020, *Phys. Rev. D*, 101, 124040  
 Dax M., Green S. R., Gair J., Macke J. H., Buonanno A., Schölkopf B., 2021, *Phys. Rev. Lett.*, 127, 241103  
 Delaunoy A., Wehenkel A., Hinderer T., Nissanke S., Weniger C., Williamson A. R., Louppe G., 2020, arXiv:2010.12931  
 Dhani A., Völkel S. H., Buonanno A., Estelles H., Gair J., Pfeiffer H. P., Pompili L., Toubiana A., 2025, *Phys. Rev. X*, 15, 031036  
 Dietrich T., Samajdar A., Khan S., Johnson-McDaniel N. K., Dudi R., Tichy W., 2019, *Phys. Rev. D*, 100, 044003  
 Essick R., 2023, *Phys. Rev. D*, 108, 043011  
 Essick R., Farr W., 2022, arXiv:2204.00461  
 Essick R., Fishbach M., 2024, *Astrophys. J.*, 962, 169  
 Estellés H., Ramos-Buades A., Husa S., García-Quirós C., Colleoni M., Haegel L., Jaume R., 2021, *Phys. Rev. D*, 103, 124060  
 Estellés H., Husa S., Colleoni M., Keitel D., Mateu-Lucena M., García-Quirós C., Ramos-Buades A., Borchers A., 2022a, *Phys. Rev. D*, 105, 084039  
 Estellés H., Colleoni M., García-Quirós C., Husa S., Keitel D., Mateu-Lucena M., Planas M. d. L., Ramos-Buades A., 2022b, *Phys. Rev. D*, 105, 084040  
 Estellés H., Buonanno A., Enficiaud R., Foo C., Pompili L., 2025, arXiv:2506.19911  
 Fairhurst S., Green R., Hoy C., Hannam M., Muir A., 2020a, *Phys. Rev. D*, 102, 024055  
 Fairhurst S., Green R., Hannam M., Hoy C., 2020b, *Phys. Rev. D*, 102, 041302  
 Fairhurst S., Hoy C., Green R., Mills C., Usman S. A., 2023, *Phys. Rev. D*, 108, 082006  
 Fairhurst S., Mills C., Colpi M., Schneider R., Sesana A., Trinca A., Valiante R., 2024, *Mon. Not. Roy. Astron. Soc.*, 529, 2116  
 Gabbard H., Messenger C., Heng I. S., Tonolini F., Murray-Smith R., 2022, *Nature Phys.*, 18, 112  
 Gamboa A., et al., 2025, *Phys. Rev. D*, 112, 044038  
 García-Quirós C., Colleoni M., Husa S., Estellés H., Pratten G., Ramos-Buades A., Mateu-Lucena M., Jaume R., 2020, *Phys. Rev. D*, 102, 064002  
 Gerosa D., Bellotti M., 2024, *Class. Quant. Grav.*, 41, 125002  
 Gerosa D., Mould M., Gangardt D., Schmidt P., Pratten G., Thomas L. M., 2021, *Phys. Rev. D*, 103, 064067  
 Goldberg J. N., MacFarlane A. J., Newman E. T., Rohrlich F., Sudarshan E. C. G., 1967, *J. Math. Phys.*, 8, 2155  
 Green S. R., Gair J., 2021, *Mach. Learn. Sci. Tech.*, 2, 03LT01  
 Green S. R., Simpson C., Gair J., 2020, *Phys. Rev. D*, 102, 104057

Guo X., Chu Q., Chung S. K., Du Z., Wen L., Gu Y., 2018, *Comput. Phys. Commun.*, 231, 62

Hamilton E., et al., 2021, *Phys. Rev. D*, 104, 124027

Hamilton E., et al., 2025, arXiv:2507.02604

Hanna C., et al., 2020, *Phys. Rev. D*, 101, 022003

Hannam M., Schmidt P., Bohé A., Haegel L., Husa S., Ohme F., Pratten G., Pürer M., 2014, *Phys. Rev. Lett.*, 113, 151101

Hannam M., et al., 2022, *Nature*, 610, 652

Harris C. R., et al., 2020, *Nature*, 585, 357

Harry I., Hoy C., 2025, arXiv: 2503.09773

Heinzel J., Vitale S., 2025, arXiv:2509.07221

Hild S., et al., 2011, *Class. Quant. Grav.*, 28, 094013

Hoy C., 2022, *Phys. Rev. D*, 106, 083003

Hoy C., Leyde K., 2025, arXiv:2511.07551

Hoy C., Raymond V., 2021, *SoftwareX*, 15, 100765

Hoy C., Mills C., Fairhurst S., 2022, *Phys. Rev. D*, 106, 023019

Hoy C., Weaving C. R., Nuttall L. K., Harry I., 2024, *Class. Quant. Grav.*, 41, 245012

Hoy C., Akcay S., Mac Uilliam J., Thompson J. E., 2025a, *Nature Astron.*, 9, 1256

Hoy C., Fairhurst S., Mandel I., 2025b, *Phys. Rev. D*, 111, 023037

Hunter J. D., 2007, *CSE*, 9, 90

Husa S., Khan S., Hannam M., Pürer M., Ohme F., Jiménez Forteza X., Bohé A., 2016, *Phys. Rev. D*, 93, 044006

Iyer B., et al., 2011, LIGO-India, Proposal of the Consortium for Indian Initiative in Gravitational-wave Observations (IndIGO), DCC, <https://dcc.ligo.org/LIGO-M1100296/public>

Kalaghatgi C., Hannam M., Raymond V., 2020, *Phys. Rev. D*, 101, 103004

Khan S., Husa S., Hannam M., Ohme F., Pürer M., Jiménez Forteza X., Bohé A., 2016, *Phys. Rev. D*, 93, 044007

Khan S., Chatzioannou K., Hannam M., Ohme F., 2019, *Phys. Rev. D*, 100, 024059

Khan S., Ohme F., Chatzioannou K., Hannam M., 2020, *Phys. Rev. D*, 101, 024056

Krishna K., Vijaykumar A., Ganguly A., Talbot C., Biscoveanu S., George R. N., Williams N., Zimmerman A., 2023, arXiv:2312.06009

Krishnendu N. V., Ohme F., 2022, *Phys. Rev. D*, 105, 064012

Lange J., O'Shaughnessy R., Rizzo M., 2018, arXiv:1805.10457

Liu Y., Du Z., Chung S. K., Hooper S., Blair D., Wen L., 2012, *Class. Quant. Grav.*, 29, 235018

London L., et al., 2018, *Phys. Rev. Lett.*, 120, 161102

Mac Uilliam J., Akcay S., Thompson J. E., 2024, *Phys. Rev. D*, 109, 084077

Maggiore M., et al., 2020, *JCAP*, 03, 050

Mandel I., Farr W. M., Gair J. R., 2019, *Mon. Not. Roy. Astron. Soc.*, 486, 1086

Matas A., et al., 2020, *Phys. Rev. D*, 102, 043023

McIsaac C., Hoy C., Harry I., 2023, *Phys. Rev. D*, 108, 123016

Mehta A. K., Olsen S., Wadekar D., Roulet J., Venumadhav T., Mushkin J., Zackay B., Zaldarriaga M., 2025, *Phys. Rev. D*, 111, 024049

Messick C., et al., 2017, *Phys. Rev. D*, 95, 042001

Metropolis N., Ulam S., 1949, Journal of the American statistical association, 44, 335

Mills C., Fairhurst S., 2021, *Phys. Rev. D*, 103, 024042

Mishra C. K., Kela A., Arun K. G., Faye G., 2016, *Phys. Rev. D*, 93, 084054

Morisaki S., 2021, *Phys. Rev. D*, 104, 044062

Morisaki S., Smith R., Tsukada L., Sachdev S., Stevenson S., Talbot C., Zimmerman A., 2023, *Phys. Rev. D*, 108, 123040

Mould M., Moore C. J., Gerosa D., 2024, *Phys. Rev. D*, 109, 063013

Mould M., Wolfe N. E., Vitale S., 2025, *Phys. Rev. D*, 111, 123049

Nitz A. H., Dent T., Dal Canton T., Fairhurst S., Brown D. A., 2017, *Astrophys. J.*, 849, 118

Nitz A. H., Dal Canton T., Davis D., Reyes S., 2018, *Phys. Rev. D*, 98, 024050

Nitz A. H., Kumar S., Wang Y.-F., Kastha S., Wu S., Schäfer M., Dhurkunde R., Capano C. D., 2023, *Astrophys. J.*, 946, 59

Olsen S., Venumadhav T., Mushkin J., Roulet J., Zackay B., Zaldarriaga M., 2022, *Phys. Rev. D*, 106, 043009

Ossokine S., et al., 2020, *Phys. Rev. D*, 102, 044055

Pan Y., Buonanno A., Taracchini A., Kidder L. E., Mroué A. H., Pfeiffer H. P., Scheel M. A., Szilágyi B., 2014, *Phys. Rev. D*, 89, 084006

Pankow C., Brady P., Ochsner E., O'Shaughnessy R., 2015, *Phys. Rev. D*, 92, 023002

Patterson B. G., Tomson S. M., Fairhurst S., 2025, *Phys. Rev. D*, 111, 044073

Pompili L., et al., 2023, *Phys. Rev. D*, 108, 124035

Pratten G., Schmidt P., Buscicchio R., Thomas L. M., 2020a, *Phys. Rev. Res.*, 2, 043096

Pratten G., Husa S., Garcia-Quiros C., Colleoni M., Ramos-Buades A., Estelles H., Jaume R., 2020b, *Phys. Rev. D*, 102, 064001

Pratten G., et al., 2021, *Phys. Rev. D*, 103, 104056

Privitera S., et al., 2014, *Phys. Rev. D*, 89, 024003

Punturo M., et al., 2010, *Class. Quant. Grav.*, 27, 084007

Pürer M., Hannam M., Ohme F., 2016, *Phys. Rev. D*, 93, 084042

Qi H., Raymond V., 2021, *Phys. Rev. D*, 104, 063031

Racine E., 2008, *Phys. Rev. D*, 78, 044021

Ramos-Buades A., Buonanno A., Estellés H., Khalil M., Mihaylov D. P., Ossokine S., Pompili L., Shiferaw M., 2023, *Phys. Rev. D*, 108, 124037

Reitze D., et al., 2019, *Bull. Am. Astron. Soc.*, 51, 035

Romero-Shaw I. M., et al., 2020, *Mon. Not. Roy. Astron. Soc.*, 499, 3295

Sachdev S., et al., 2019, arXiv:1901.08580

Schmidt P., Ohme F., Hannam M., 2015, *Phys. Rev. D*, 91, 024043

Singh M. K., Kapadia S. J., Vijaykumar A., Ajith P., 2024, *Astrophys. J.*, 971, 23

Singh M. K., Patterson B. G., Fairhurst S., 2025, arXiv:2512.07688

Skilling J., 2004, in AIP Conference Proceedings. AIP, doi:10.1063/1.1835238, <https://doi.org/10.1063/1.1835238>

Skilling J., 2006, *Bayesian Analysis*, 1, 833

Smith R., Field S. E., Blackburn K., Haster C.-J., Pürer M., Raymond V., Schmidt P., 2016, *Phys. Rev. D*, 94, 044031

Speagle J. S., 2020, *Mon. Not. Roy. Astron. Soc.*, 493, 3132

Talbot C., Golomb J., 2023, *Mon. Not. Roy. Astron. Soc.*, 526, 3495

Talbot C., Thrane E., 2018, *Astrophys. J.*, 856, 173

Talbot C., Smith R., Thrane E., Poole G. B., 2019, *Phys. Rev. D*, 100, 043030

Thomas L. M., Schmidt P., Pratten G., 2021, *Phys. Rev. D*, 103, 083022

Thompson J. E., Fauchon-Jones E., Khan S., Nitoglia E., Pan-narale F., Dietrich T., Hannam M., 2020, *Phys. Rev. D*, 101, 124059

Thompson J. E., Hamilton E., London L., Ghosh S., Kolitsidou P., Hoy C., Hannam M., 2024, *Phys. Rev. D*, 109, 063012

Thompson J. E., Hoy C., Fauchon-Jones E., Hannam M., 2025, *Phys. Rev. D*, 112, 064011

Thorne K. S., 1980, *Rev. Mod. Phys.*, 52, 299

Thrane E., Talbot C., 2019, *Publ. Astron. Soc. Austral.*, 36, e010

Tiwari V., 2018, *Class. Quant. Grav.*, 35, 145009

Tiwari V., Hoy C., Fairhurst S., MacLeod D., 2023, *Phys. Rev. D*, 108, 023001

Ursell R., Hoy C., Harry I., Nuttall L. K., 2025, arXiv:2510.15048

Usman S. A., et al., 2016, *Class. Quant. Grav.*, 33, 215004

Varma V., Field S. E., Scheel M. A., Blackman J., Gerosa D.,

Stein L. C., Kidder L. E., Pfeiffer H. P., 2019a, *Phys. Rev. Research.*, 1, 033015

Varma V., Field S. E., Scheel M. A., Blackman J., Kidder L. E., Pfeiffer H. P., 2019b, *Phys. Rev. D*, 99, 064045

Veitch J., et al., 2015, *Phys. Rev. D*, 91, 042003

Vinciguerra S., Veitch J., Mandel I., 2017, *Class. Quant. Grav.*, 34, 115006

Virtanen P., et al., 2020, *Nature Methods*, 17, 261

Vitale S., Mould M., 2025, *Phys. Rev. D*, 112, 083015

Vitale S., Gerosa D., Farr W. M., Taylor S. R., 2020, [arXiv:2007.05579](https://arxiv.org/abs/2007.05579)

Williams M. J., 2025, arXiv: 2511.04218

Williams M. J., Karamanis M., Luo Y., Seljak U., 2025, *Mon. Not. Roy. Astron. Soc.*, 1479, 1493

Wolfe N. E., Mould M., Heinzel J., Vitale S., 2025, [arXiv:2510.06220](https://arxiv.org/abs/2510.06220)

Wysocki D., Lange J., O'Shaughnessy R., 2019, *Phys. Rev. D*, 100, 043012

Yelikar A. B., Shaughnessy R. O., Lange J., Jan A. Z., 2024, *Phys. Rev. D*, 110, 064024

Zackay B., Dai L., Venumadhav T., 2018, [arXiv:1806.08792](https://arxiv.org/abs/1806.08792)

## APPENDIX A: METHODS

### A1 Single event Bayesian inference

Bayesian inference is the process of inferring the properties  $\theta$  of a model  $\mathfrak{M}$  given some observed data  $d$ . The probability of *e.g.* the binary black hole having parameters  $\theta$  is obtained through Bayes theorem,

$$P(\theta|d, \mathfrak{M}) = \frac{\mathcal{L}(d|\theta, \mathfrak{M}) \Pi(\theta|\mathfrak{M})}{\mathcal{Z}}, \quad (\text{A1})$$

where  $\mathcal{L}(d|\theta, \mathfrak{M})$  is the probability of the data given the parameters  $\theta$  and model  $\mathfrak{M}$ , otherwise known as the likelihood,  $\Pi(\theta|\mathfrak{M})$  is the probability of the parameters  $\theta$  given the model  $\mathfrak{M}$ , otherwise known as the prior and  $\mathcal{Z} = \int (\mathcal{L}(d|\theta, \mathfrak{M}) \Pi(\theta|\mathfrak{M})) d\theta$  is the evidence or marginal likelihood. When Bayesian inference is performed with multiple models, the evidence can be used to quantify the support for one model over the other through the Bayes factor,

$$\mathcal{B} = \frac{\mathcal{Z}_1}{\mathcal{Z}_2}, \quad (\text{A2})$$

where  $\mathcal{Z}_1$  is the evidence for  $\mathfrak{M}_1$  and  $\mathcal{Z}_2$  is the evidence for  $\mathfrak{M}_2$ . An alternative technique is to sample over the models as part of the inference (Hoy 2022). This has the advantage that model accuracy can then be incorporated (Hoy et al. 2025a).

It is often not possible to analytically calculate the posterior distribution. Instead, stochastically sampling techniques, such as nested sampling (Skilling 2004, 2006) or Markov Chain Monte-Carlo (Metropolis & Ulam 1949), are often employed to obtain *samples* from the unknown posterior distribution; although alternative methods have been proposed in the literature (Pankow et al. 2015; Lange et al. 2018; Delaunoy et al. 2020; Green et al. 2020; Chua & Valisneri 2020; Green & Gair 2021; Dax et al. 2021; Gabbard et al. 2022; Tiwari et al. 2023; Fairhurst et al. 2023; Williams et al. 2025). Numerous packages are available for performing Bayesian inference on GW signals (Veitch et al. 2015; Ashton et al. 2019; Romero-Shaw et al. 2020; Biwer et al. 2019). In

this work, we use `bilby` (Ashton et al. 2019; Romero-Shaw et al. 2020), and employ the `dynesty` (Speagle 2020) nested sampler.

When analysing simulated GW signals  $h$  injected into idealised Gaussian noise  $n$  – such that  $d = h + n$  – we use wide and agnostic priors that follow the conventions adopted by the LVK. Specifically in this work, we sample uniformly in component masses between a chirp mass  $2 M_\odot < \mathcal{M} < 200 M_\odot$  and mass ratio  $0.05 < q < 1$ . The luminosity distance is also assumed to be uniform in volume between  $10 \text{ Mpc} < d_L < 10000 \text{ Mpc}$ . All other parameters are assumed to be agnostic within their regions of validity. Given the wide prior volume, we use 2000 live points to ensure robust results. Although numerous methods have been developed to accelerate likelihood evaluations, we use the full Whittle likelihood in this work.

### A2 Population inference

Once a catalog of observations has been made  $\mathcal{D}$ , Hierarchical Bayesian inference can be used to infer the underlying properties of the population  $\lambda$ . The probability of *e.g.* the catalog of binary black holes following a mass and spin distribution with hyperparameters  $\lambda$  is similarly obtained through Bayes theorem,

$$P(\lambda|\mathcal{D}) = \frac{\mathcal{L}(\mathcal{D}|\lambda) \Pi(\lambda)}{p(\mathcal{D})}, \quad (\text{A3})$$

where  $\mathcal{L}(\mathcal{D}|\lambda)$  is the hierarchical likelihood,  $\Pi(\lambda)$  is the hyperparameter prior, and  $p(\mathcal{D})$  is evidence. Assuming all GW signals are of astrophysical origin and all noise realizations are independent, the hierarchical likelihood is (Mandel et al. 2019; Vitale et al. 2020; Abac et al. 2025b),

$$\mathcal{L}(\mathcal{D}|\lambda) = \prod_{i=0}^N \frac{\int P(d_i|\theta) P(\theta|\lambda) d\theta}{\int p_{\text{det}}(\theta) P(\theta|\lambda)} \quad (\text{A4})$$

where  $N$  is the number of observed events in the catalog,  $d = \mathcal{D}_i$  and corresponds to the  $i$ th event in the catalog,  $P(\theta|\lambda)$  specifies the distribution of binary black hole parameters  $\theta$  given the mass and spin model with parameters  $\lambda$ , and  $p_{\text{det}}(\theta)$  is the detection probability of an event with parameters  $\theta$ . It is crucial to include the detection probability in the denominator as current template-based search pipelines adopted by the LVK (Cannon et al. 2012; Privitera et al. 2014; Messick et al. 2017; Hanna et al. 2020; Sachdev et al. 2019; Usman et al. 2016; Nitz et al. 2017, 2018; Adams et al. 2016; Chu et al. 2022; Liu et al. 2012; Guo et al. 2018) are more likely to observe GW signals from *e.g.* high mass binaries than low mass binaries due to the increase in sensitive volume. The integrals in Eq. A4 are typically approximated through Monte Carlo sums (Tiwari 2018).

Often the detection probability is determined by injecting  $\mathcal{O}(10^8)$  simulated GW signals into real detector noise, and identifying the fraction of signals identified from the (currently adopted) search pipelines (Abac et al. 2025c). In this work, we simplify the process by assuming all signals with total power greater than 12 are detected (Essick & Fishbach 2024; Agarwal et al. 2025; Hoy & Leyde 2025). While the detection probability depends on the waveform model (used when simulating the GW signals), we expect

Threshold ( $\rho_{\text{thres}}$ )	Reduction in computational cost [%]
0	-
0.5	2
1.0	6
1.5	20
2.0	25
2.5	40
3.0	45

**Table B1.** Table showing the reduction in computational cost of performing Bayesian inference for a worst-case scenario population of 90 events for different SNR thresholds,  $\rho_{\text{thres}}$ . We compare to the computational cost when consistently using XPHM for all events,  $\rho_{\text{thres}} = 0$ . For  $\rho_{\text{thres}} = 0$ , the total computational cost of analysing our population was 50 CPU years.

any differences to be small. We therefore neglect this systematic error.

When performing Hierarchical Bayesian inference in this work, we assume a POWERLAW+PEAK distribution (Abbott et al. 2021) for the primary component mass and a powerlaw for the mass ratio. The spin magnitudes are assumed to be independently and identically drawn from a Beta distribution (Wysocki et al. 2019), and a mixture model is used for the spin tilt (Talbot & Thrane 2018). Similar to single-event Bayesian inference, we use stochastic sampling to obtain posterior samples from the unknown hyperposterior. We use `gwpopulation` (Talbot et al. 2019), and employ the `dynesty` (Speagle 2020) nested sampler with 1000 live points. We assume wide and agnostic priors for all hyper parameters  $\lambda$ . Specifically, we assume that the powerlaw for the primary mass is uniform between  $-4 < \alpha < 12$  and the powerlaw for the mass ratio is uniform between  $-5 < \beta_q < 12$ . The minimum primary mass is assumed to be uniform between  $2 M_\odot < m_{\min} < 10 M_\odot$ , while the maximum is allowed to vary uniformly between  $30 M_\odot < m_{\max} < 100 M_\odot$ . For the spin magnitude distribution, we assume both parameters of the Beta distribution are uniform between  $0 < \alpha_\chi < 10$  and  $0 < \beta_\chi < 10$ .

## APPENDIX B: ALTERNATIVE SNR THRESHOLDS

In the main text, we highlighted the inferred mass and spin distribution for two SNR thresholds,  $\rho_{\text{thres}} = 1.5$  and  $\rho_{\text{thres}} = 2.0$ . Here, we show the results for SNR thresholds  $\rho_{\text{thres}} \in [0, 0.5, 1.0, 1.5, 2.0, 2.5, 3.0]$ .

In Fig. B1 we see that the inferred mass distribution remains comparable for different SNR thresholds. Focusing on the mass ratio distribution, we see that as the threshold increases, there is marginally more support for asymmetric binaries;  $\beta_q$  has larger support for negative values as  $\rho_{\text{thres}}$  increases. This implies that even for binaries with some evidence for precession and higher order multipoles, XAS can be used (alongside other models for candidates with significant evidence for precession and higher order multipoles), and is sufficient for capturing the mass distribution. This is consistent with the conclusions found in Singh et al. (2024). As the threshold increases further, such that XAS is being used for all GW candidates, biases begin to be observed in

the mass distribution, particularly in the inferred powerlaw of the primary mass. This is consistent with the conclusions found in Hoy & Leyde (2025).

The same is not true for the inferred spin distribution. We see that as  $\rho_{\text{thres}}$  increases, biases are observed in the spin magnitude and spin tilt distributions, with the spin magnitude marginally underestimated, and the spin tilts favouring more aligned configurations. This is expected from the reweighting and conditioning technique we adopted to predict the spin tilt distribution for XAS, see Fig. 4. Since we are only conditioning on the observed  $\chi_{\text{eff}}$ , we are neglecting any measurable power from the in-plane spins and any contribution from the mass ratio (Baird et al. 2013).

In Tab. B1 we provide a comparison of the runtimes for different SNR thresholds. We see that as the threshold increases, there is a greater reduction in computational cost compared to consistently using XPHM for all analyses. This is expected since a greater fraction of events will be analysed with computationally cheaper models.

## APPENDIX C: A MISIDENTIFIED SIGNAL

In Sec. 3, we highlighted that `simple-pe` can be used to directly extract  $\rho_p$  and  $\rho_{\text{HM}}$  from the GW strain data through matched filtering. We then compared the true and matched filter SNRs and highlighted that in 6% of cases, we obtain false negatives. This means that our selection function may have mis-selected XAS compared to XPHM, XP or XHM. Here, we show the impact of misidentifying the significance of the signal on the inferred parameter estimates. We consider an injection that has significant evidence for spin-precession,  $\rho_p \sim 3.5$ , yet we obtain a matched filter SNR of  $\sim 1.5$  through `simple-pe`. This injection had component masses  $m_1 = 14 M_\odot, m_2 = 13 M_\odot$ , spin magnitudes  $\chi_1 = 0.6, \chi_2 = 0.8$  and observed at a network SNR of 17 in LIGO-Hanford and Virgo. The effective parallel spin was  $\chi_{\text{eff}} = 0.1$  and the effective perpendicular spin was  $\chi_p = 0.7$ .

Fig. C1 shows the inferred posterior distribution for XPHM and XAS, after reweighting to a uniform spin magnitude prior and conditioning based on the observed  $\chi_{\text{eff}}$ , see Sec. 4 and Fig. 4 for details. We see that XAS and XPHM both recover the primary mass and mass ratio well. XPHM obtains a more precise distribution, as expected. We see a larger difference for the inferred effective spins, but importantly both XAS and XPHM recover the true value within the 90% credible interval. We see that XAS obtains a wider distribution for  $\chi_{\text{eff}}$  with less support for larger effective perpendicular spins. This is expected from the reweighting and conditioning procedure, as we ignore any measurable evidence of precession.

The inferred 90% credible interval scales with the total signal power: as the SNR increases, the inferred 90% credible interval narrows for all models. If this injection had  $\text{SNR} > 20$  it is likely that XAS would recover a biased distribution for the spins. This begs the question of whether or not we should include the network SNR when determining the selection threshold. For example, we could always use XPHM if the total signal power is greater than *e.g.* 20, even if the matched filter  $\rho_p < \rho_{\text{thres}}$  and  $\rho_{\text{HM}} < \rho_{\text{thres}}$  to avoid this issue. This would also alleviate additional concerns from the improved measurement from XPHM due to

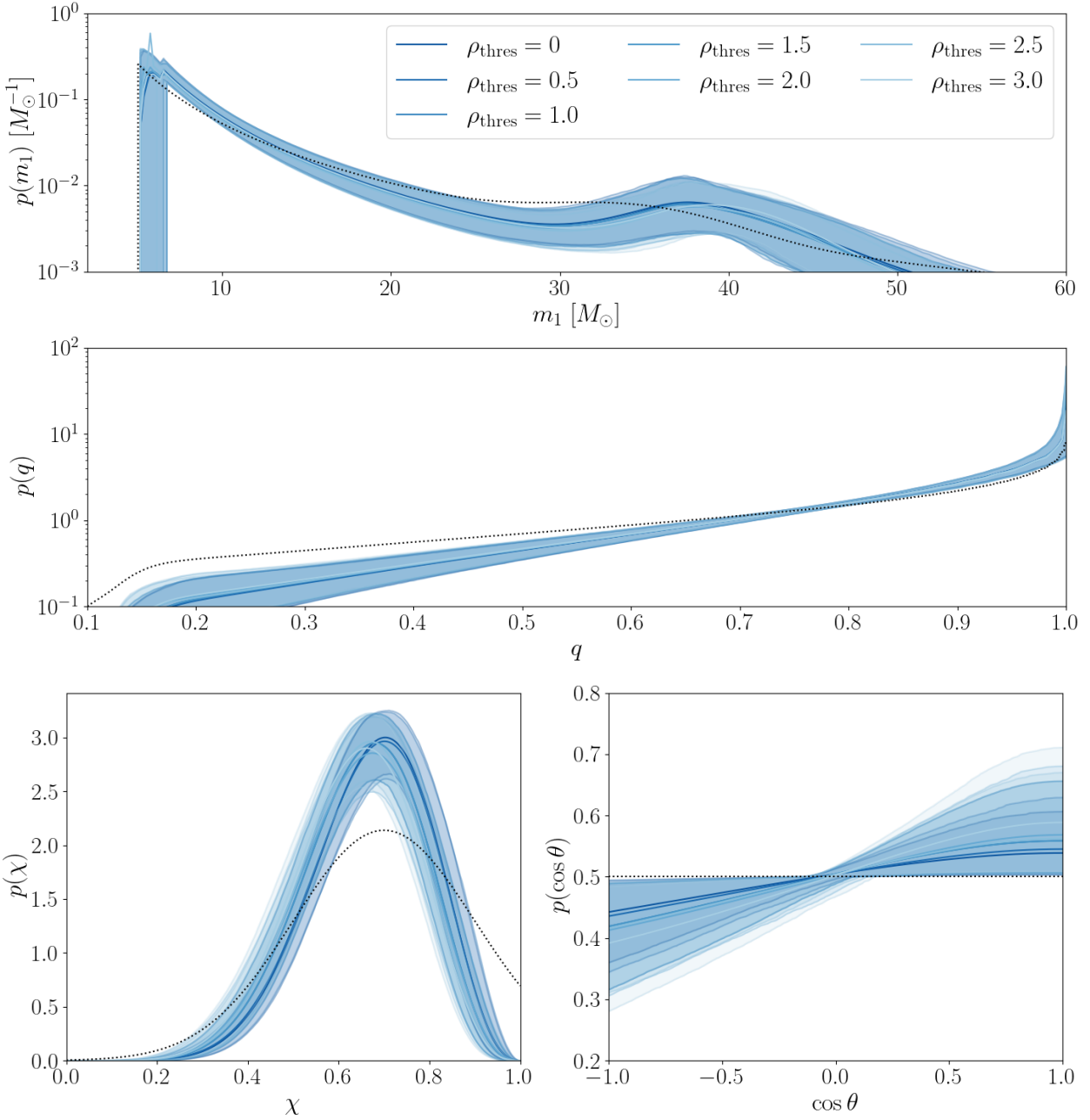


**Figure B1.** Plot similar to Fig. 5 except we now show the inferred mass and spin distribution for different SNR thresholds  $\rho_{\text{thres}}$ . In this work, we recommend using  $\rho_{\text{thres}} = 1.5$  for robust results.  $\rho_{\text{thres}} = 0$  corresponds to XPHM in Fig. 5.

no evidence for precession and higher order multipoles, as discussed in Sec. 2.3. However, we highlight that even without this additional constraint, we obtain comparable mass and spin distributions for the underlying properties of black holes for a worst-case scenario population. This implies that this additional constraint, which would reduce the computational efficiency of our approach, may not be necessary for population level measurements.

#### APPENDIX D: A GWTC-LIKE POPULATION

In the main text, we considered a worst-case scenario population containing highly spinning binary black holes with a preference for asymmetric component masses. Here, we consider an astrophysically motivated population of binary black holes. This population represents the signals observed by the LVK: a ‘GWTC-like’ population. Since this population contains fewer events with observable spin-precession and higher order multipole power (Hoy et al. 2025b), we expect to obtain consistent mass and spin distribution when imposing our recommended SNR threshold of  $\rho_{\text{thres}} = 1.5$ . This is further supported by the conclusions in Singh et al.

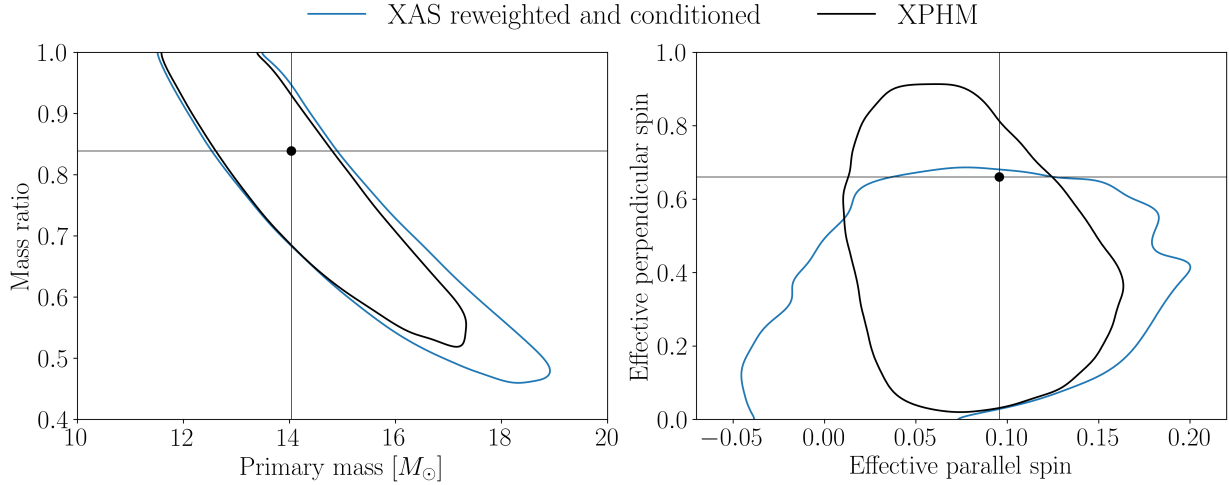


**Figure C1.** Plot showing the inferred *Left*: primary mass and mass ratio and *Right*: effective parallel spin  $\chi_{\text{eff}}$  and effective perpendicular spin  $\chi_p$  when performing Bayesian inference on a misidentified GW signal; a signal that we identify as having no evidence for spin-precession despite there being strong observable features. This injection corresponds to a false negative in Fig. 3. The GW signal was produced with XPHM into idealised Gaussian noise. The black cross hairs show the true values and the contours show the inferred 90% credible interval. The reweighting and conditioning technique applied to XAS is described in Sec. 4 and Fig. 4.

(2024); Hoy & Leyde (2025); Fig. 5 in Singh et al. (2024) demonstrated that neglecting higher order multipoles will not cause a significant bias in the population inference for a catalog of 750 simulated signals, and Figs. 3 and 9 in Hoy & Leyde (2025) demonstrated that for an astrophysically motivated population of 100 signals, neglecting precession will not cause a significant bias in the population inference.

We obtain our simulated population by assuming that the mass ratio follows a power law  $q^{\beta_q}$  with index  $\beta_q = 1.1$ , and a uniform distribution for the spin magnitudes. We also assume that the primary mass follows a truncated power law with index  $\alpha = -2.3$ , between a minimum,  $m_{\min} = 5 M_\odot$ , and maximum  $m_{\max} = 80 M_\odot$  mass. We assume that there is a Gaussian component in the mass distribution at  $m_1 = 34 M_\odot$ , with relative weight  $\lambda = 0.038$  and standard deviation  $\sigma_g = 5 M_\odot$ .

As expected, we obtain conclusions similar to those in the main text: the mass distribution remains comparable to XPHM for the SNR thresholds considered. However, we see marginal differences in the spin distribution. Namely, a preference for more aligned spin binaries. In Fig. D1 we show a corner plot comparing the hyper posteriors for the mass distribution against their true values.

This paper has been typeset from a T<sub>E</sub>X/L<sub>A</sub>T<sub>E</sub>X file prepared by the author.

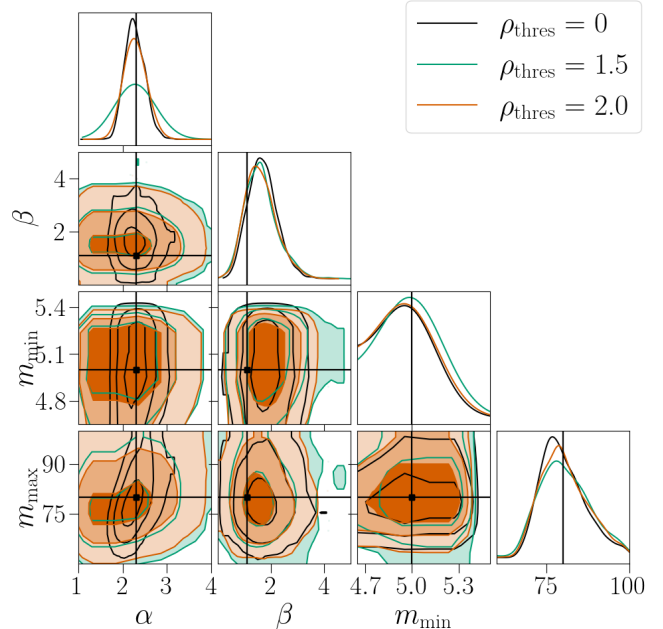


**Figure D1.** Corner plot showing a subset of the inferred hyper parameters controlling the mass distribution of black holes. We consider a GWTC-like population with a uniform distribution of spins, see App. D for details. The black cross hairs show the true values.